90°-CAVITIES WITH IMPROVED INNER-CELL HOM PROPERTIES

Shannon Hughes

University of Notre Dame, South Bend, IN 46556

Valery Shemelin

Laboratory for Elementary-Particle Physics, Cornell University, Ithaca, NY 14853

Abstract

In order to reduce non-propagating ("trapped") higher-order modes in multicell cavities with 90° cell wall slope angles, attempts were made to modify cavity geometry so as to broaden the bandwidths of these modes. The best geometry modifications were determined for both broadening the bandwidth of a single mode and broadening the net bandwidth of the first seven modes, and these modifications yielded results comparable with existing TESLA and ERL shapes.

INTRODUCTION

When an SRF cavity is created, its geometry is fitted for a working π-mode frequency [1]. However, the geometry of a cavity is very exact and can be difficult to fabricate precisely. As a result, even in a very well-made multicell cavity there will be many minor defects in each cell. The problem is that slight changes to any of a cavity's geometric parameters, even on the order of less than 1 mm, can alter the frequency of a mode – sometimes drastically. If the altered frequency is not a propagating frequency, then the mode is trapped. For higher-order modes (HOMs), this means that the mode cannot travel from the inner cells to the damping couplers, and its energy cannot be removed. To avoid this unfortunate consequence, it is important to stop trapped modes from occurring.

One way to stop modes from becoming trapped is to increase the bandwidth of each mode until all modes are as broad as possible. By increasing the range of frequencies at which propagation occurs in a mode, we reduce the potential for trapping, in spite of any imperfections a cavity might have. In this way, a cavity's geometry can be "tuned". Work has already been done to tune the end cells for extraction [2], but in this paper, methods for broadening a single mode and for a net broadening of all modes are explored for the inner cells.

Throughout this broadening of bandwidths, the cell wall slope angle of the cavity, α, is kept at 90°, as this angle is determined to be the best compromise of function and practicality. That is, although a reentrant cavity shape (with a wall slope angle less than 90°) will theoretically perform best, a non-reentrant cavity (with an angle greater than 90°) will be easier to build and use. The 90° shape, neither reentrant nor non-reentrant (as shown in Fig. 1), offers the best qualities of both. Furthermore, this cavity shape is interesting because it has also been studied and implemented by other researchers. The LSF, NLSF, and

Ichiro cavities, for instance, all have a cell wall slope angle of 90° [3, 4]. As such, these cavities can be useful to us for comparison purposes.
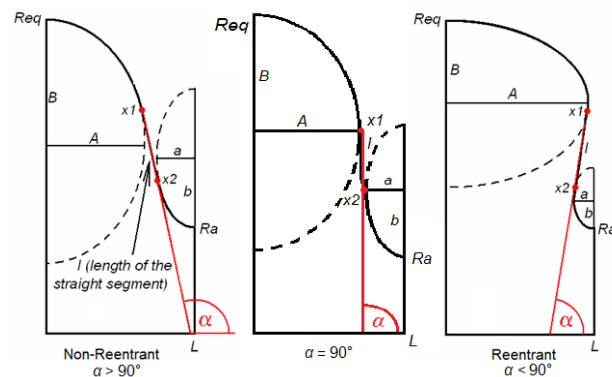

Figure 1. Cavity geometry from non-reentrant, reentrant, and 90° shapes, with elliptic arc parameters A, B, a, and b shown.

PROGRAMS USED

SLANS

SLANS [5] was used to calculate figures of merit of the fundamental (monopole) mode for cells with different wall slope angles and phase shifts. Additionally, SLANS was used to plot electric field vectors for each geometry.

SLANS2

SLANS2 [5] was used to calculate figures of merit of the HOM (dipole) modes for cells with different wall slope angles and phase shifts. Additionally, SLANS2 was used to plot electric field vectors for each geometry, see Appendix.

TunedCell

TunedCell [6], a wrapper program for SLANS and SLANS2, was used, like these two programs, to calculate e, h (defined below), and many other figures of merit for a given set of elliptic arc parameters. This program was also used to create half-cell geometry files.

MathCAD

MathCAD was used to create graphs and fit spline curves to data, create multicell and single-cell geometry files, and to generate the random numbers used for the Monte Carlo technique.
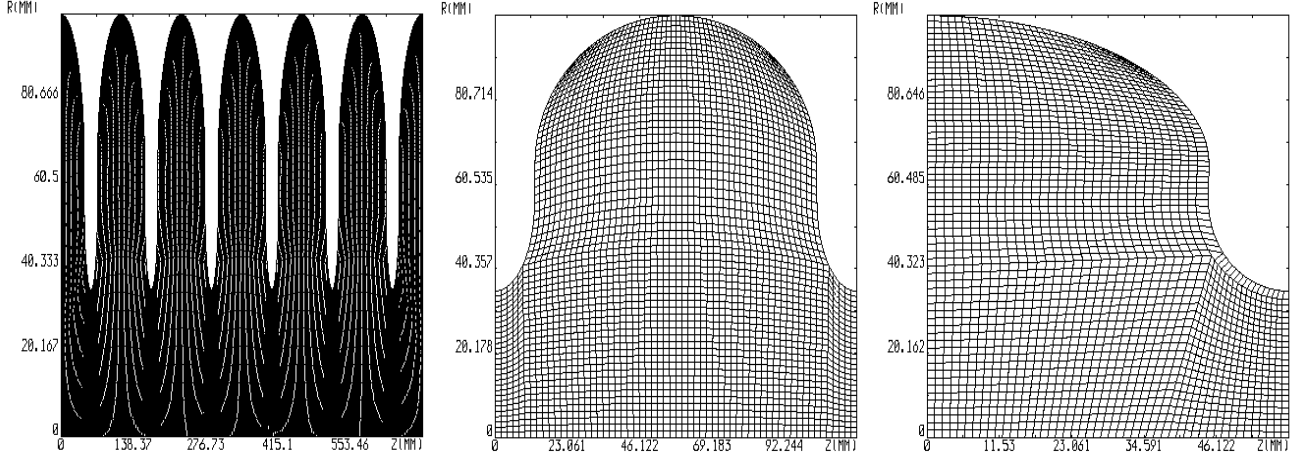
Fig 2. Six-cell, single-cell, and half-cell cavity meshes created using TunedCell and SLANS.

GEOMETRY USED

Fig. 2 shows the meshes created for each of the three types of cavity geometry used in this paper – six-cell, single-cell, and half-cell. The six-cell geometry was used when it was necessary to calculate many phase shifts between 0 and π modes – for instance, when plotting dispersion curves. The single- or half-cell cavities were used for efficiency when only the 0 and π modes were thought to be necessary, such as when calculating the bandwidths of higher-order modes.

FUNDAMENTAL MODE

For easier comparison with the well-known TESLA cavity shape (which is also the prototype for the ILC), we will use the following normalized values: $e = E_{pk}/2E_{acc}$, where E_{pk} is the maximal electric field and E_{acc} is the accelerating field, and $h = H_{pk}/42E_{acc}$, where H_{pk} is the maximal magnetic field. The coefficients 2 and 42 (Oersted/(MV/m)) are chosen so that e and h are close to 1 for the TESLA shape.

The frequencies shown in Fig. 3 were calculated using SLANS at an accuracy level of $1.0 \cdot 10^{-6}$ (in frequency) to analyze six-cell meshes with geometries optimized for minimum h. For a set of geometries optimized for minimum h, the shapes with smaller wall slope angles generally have the largest bandwidths for a given e, where bandwidth is defined to be the difference between the frequency of the π-mode and the 0-mode ($B_0 = f_\pi - f_0$). For the fundamental mode, this is important because a larger bandwidth means that the difference in frequency between the π-mode and the mode nearest to it (for example, the $6\pi/7$ mode when end-cells are added to the six-cell inner portion) will be greater, making it easier to tune for the working π-mode frequency.
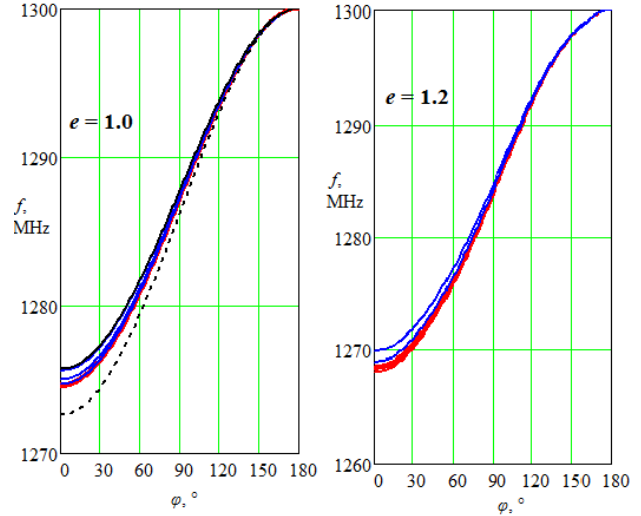

Figure 3. Dispersion curves plotting the dependence of frequency on phase shift, φ, for $e = 1.0$ (left) and $e = 1.2$ (right). Geometries with $\alpha \leq 90°$ are plotted in red while those with $\alpha > 90°$ are plotted in blue. TESLA is plotted as a thick black line (the upper curve) while ERL is plotted as a dashed black line, both on the $e = 1.0$ graph.

In terms of cell-to-cell coupling, as well, cavities with smaller wall slope angles generally yield better results than those with larger wall slope angles. Moreover, despite concerns about cell-to-cell coupling in reentrant cavities, these cavities produce equally good if not better results than their non-reentrant counterparts, as shown in Table 1. Cell-to-cell coupling (k) is calculated using the following equation:

Table 1. Parameters of several cells optimized for min h, with ERL and TESLA cells included for comparison.

$e = 1.0$	α,°	B_0, MHz	k, %	h
Reentrant	82.70	25.336	1.968	0.9500
	85	25.450	1.977	0.9502
90°	90	25.442	1.976	0.9523
Non-Reentrant	95	25.301	1.965	0.9579
	100	24.987	1.941	0.9701
	105	24.399	1.894	0.9947
ERL (e=1.0018)	102.366	27.353	2.126	0.9826
TESLA (e=0.9938)	103.354	24.290	1.886	0.9902
$e = 1.2$	α,°	B_0, MHz	k, %	h
Reentrant	67.79	31.440	2.448	0.8997
	70	31.317	2.457	0.8997
	75	31.507	2.468	0.9006
	80	31.931	2.471	0.9028
	85	31.662	2.466	0.9067
90°	90	31.468	2.444	0.9135
Non-Reentrant	95	30.899	2.406	0.9246
	100	30.071	2.340	0.9410
	105	28.866	2.245	0.9664

As shown in Fig. 4 and Table 1, the difference in coupling value between the best reentrant shape and the 90° shape is very small, especially in the $e = 1.0$ case, where the best reentrant k-value is 1.977 and the 90° k-value is 1.976, a difference of only 0.001. For $e = 1.2$, the difference between the best reentrant and 90° k-value is only 0.027. These small differences suggest that the 90° shape has only small and perhaps imperceptible disadvantages compared with the reentrant shape.
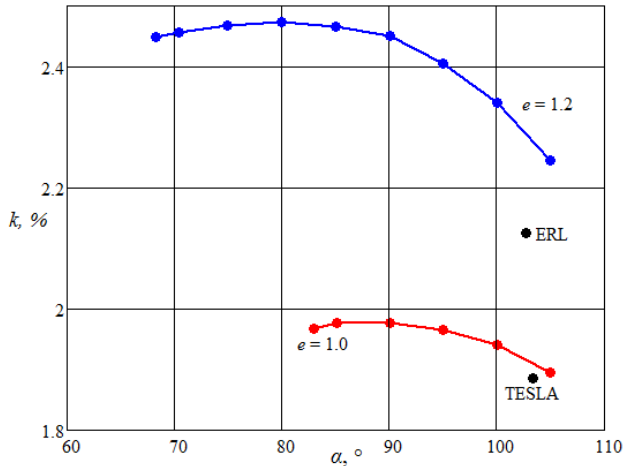

Figure 4. Plot showing the cell-to-cell coupling for various wall slope angles for ERL, TESLA, e=1.0, and e=1.2 cavities.

Because $e = 1$ is the most common case (ERL, TESLA), we will study this case more thoroughly. Let us imagine a reference cavity with $e = 1$, $h = 1$ and B_0 and k identical to TESLA values. Table 2 shows how each of the $e = 1$ cavities described above differ from such a reference cavity.

Table 2. Increase in B_0, h, and k for several cells compared to reference cavity.

$e = 1$	α,°	ΔB_0, MHz	Δk, %	Δh
Reentrant	82.70	1.046	0.082	-0.0500
	85	1.160	0.091	-0.0498
90°	90	1.152	0.090	-0.0477
Non-Reentrant	95	1.011	0.079	-0.0421
	100	0.697	0.055	-0.0299
	105	0.109	0.008	-0.0053
ERL (e=1.0018)	102.693	3.063	0.240	-0.0174
TESLA (e=0.9938)	103.354	0.000	0.000	-0.0098

From Table 2, one can see that the improvement of h from $\alpha = 105°$ to $\alpha = 90°$ is 0.0424 while the improvement of h from $\alpha = 90°$ to $\alpha = 82.70°$, the limiting angle, is only 0.0023. So 94.9% of the total improvement in h occurs from 105° to 90°.
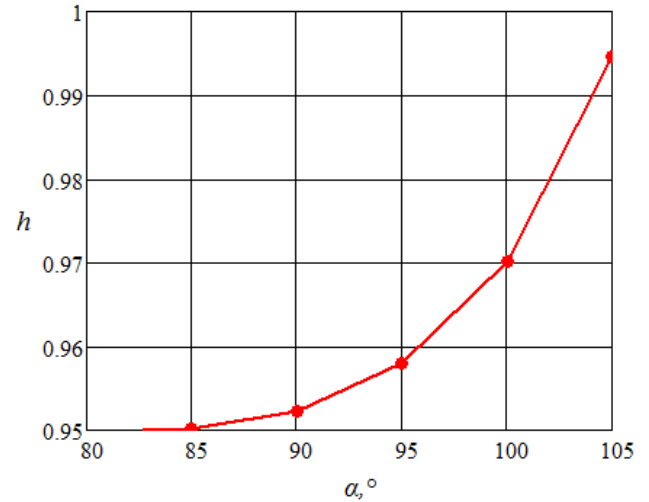

Figure 5. Plot showing dependence of h on α when $e = 1$.

That is, although h continues to improve as α decreases, gains tend to become much smaller below 90°, as Fig. 5 shows. This suggests that in terms of h, as well, the 90° shape will only have a slight disadvantage when compared with reentrant shapes.

Additionally, the 90° shape has definite practical advantages compared with the reentrant shape. Reentrant cavities have the unfortunate property of trapping water and chemicals or gases during chemical treatment or rinsing which cannot be easily removed due to their inward curving shape. Moreover, the reentrant shape is somewhat more complicated in fabrication. The 90° shape, however, does not share these problems despite, as described above, yielding almost identical results for bandwidth, cell-to-cell coupling, and h value in the $e = 1$

case. Since the 90° cavity performs just as well as the reentrant cavity, we can use this shape to enjoy some of the reentrant cavity's benefits without its drawbacks.
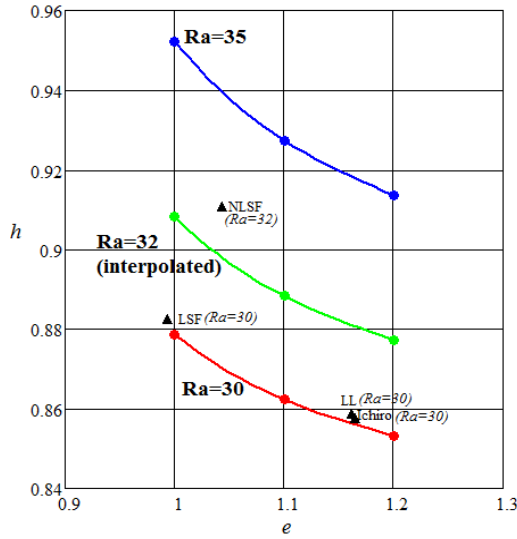

Figure 6. Plot showing h vs e for our normalized curves and for various other 90°-cavities [3,4].

Furthermore, our particular 90°-cavities compare favorably to other 90°-cavities created by other groups, such as the NLSF, LSF, LL, and Ichiro cavities [3,4] shown in Fig. 6. From the plot, it is clear that these other cavities fall at or below our curves for each value of R_a (radius of cavity aperture). That is, for a given value of e they have a greater or equal value of h than our cavities. This indicates that our cavity geometry will be a good starting point for broadening modes, as it is already optimized for other figures of merit.

DIPOLE MODES

Broadening One Dipole Mode

The frequencies shown in Fig. 7 and Fig. 8 were again calculated using SLANS at an accuracy level of $1.0 \cdot 10^{-6}$ to analyze six-cell geometries created using MathCAD. In the 1st dipole mode, the bandwidths for the 90°- and reentrant cavities are larger than the ERL and TESLA bandwidths, in addition to being very similar to one another, as shown in Fig 7.

For the 3rd dipole mode, however, the TESLA and ERL bandwidths remain relatively large (106.810 MHz and 105.792 MHz) while the 90° and reentrant bandwidths shrink to 13.105 and 6.056 MHz, respectively, as shown in Fig 7. Clearly these bandwidths need to be improved if either 90°- or reentrant cavities are to be used at this frequency.
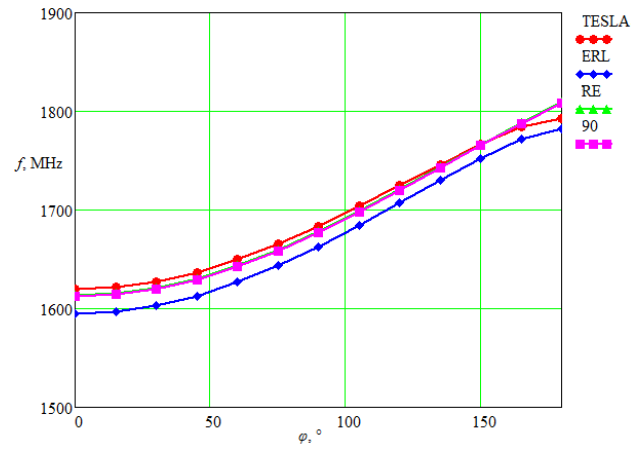

Figure 7. Dispersion curve plotting dependence of frequency on phase shift, φ, for the 1st dipole mode for several geometries.
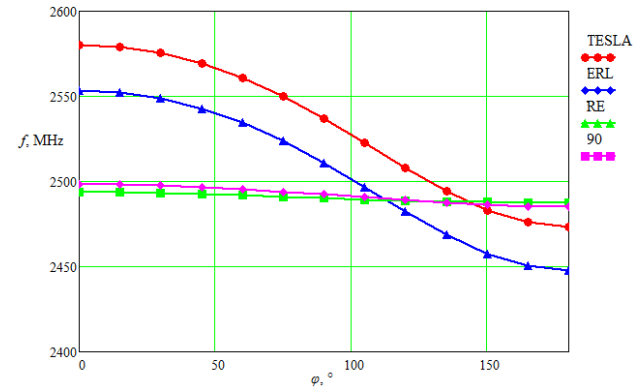

Figure 8. Dispersion curve plotting frequency against phase shift for the 3rd dipole mode for several geometries.

In order to improve the 90°-cavity's bandwidth, the derivatives of bandwidth with respect to three of the four elliptic arc parameters (A, B, and b) were calculated. Additionally, the derivatives of e and h with respect to the elliptic arc parameters were found, as well as the derivatives of bandwidth with respect to e and h. All of these derivatives were calculated from the same initial point: the 90° wall slope cavity with $e = 1$. The calculations were done by modifying each elliptic arc parameter (separately) by 0.01 mm and using TunedCell to calculate the changes in each of the variables, which were used to create a single-cell geometry file with MathCAD. The geometry file was then analyzed by SLANS2 in order to obtain f_π and f_0 at an accuracy level of $1.0 \cdot 10^{-6}$ and ultimately determine the change in bandwidth (B_3). A single-cell rather than six-cell geometry file was used in this case because it was thought that the only frequencies necessary to calculate bandwidth were f_π and f_0, so only one phase shift was thought to be necessary. A case where this does not hold true is examined later in the paper.

Then the change in, for instance, bandwidth, was divided by the change in A in order to obtain a derivative. The fourth elliptic arc parameter, a, was treated as a dependent variable throughout these calculations (and throughout the rest of this paper), held at $a = L - A$ (where L is half the length of the cavity, 57.6524 mm) in order to maintain a wall slope angle of 90°. The results of these calculations are shown in Table 3.

Table 3. Results of small changes to elliptic arc parameters A, B, and b. Effects on limiting factors e and h as well as derivatives with respect to these parameters are shown.

	B_3	e	h	$\partial B_3/\partial\_$	$\partial h/\partial\_$	$\partial e/\partial\_$
$\Delta A= 0.01$	11.872	1.000246	0.952236	-15.300	-0.0070	0.0255
$\Delta B= 0.01$	12.075	0.999998	0.952319	5.000	0.0013	0.0007
$\Delta b= 0.01$	12.048	0.999991	0.952315	2.300	0.0009	0.0000

From Table 3, it is clear that changing A has the greatest effect on the bandwidth. So the first method used to widen the bandwidth was incrementally changing A in the direction of increasing bandwidth while recording the change in the other variables. It was decided that e and h should not be allowed to increase more than 5% from their initial values, meaning that e should not exceed 1.04999 and h should not exceed 0.999213. A was increased until one of these values was exceeded, as shown in Table 4.

Table 4. Results of incrementally decreasing A. Effects on limiting factors e and h as well as derivatives with respect to A are shown.

ΔA	B_3	e	h	$\partial B_3/\partial A$	$\partial h/\partial A$	$\partial e/\partial A$
-0.10	13.362	0.997279	0.953427	-13.370	-0.0112	0.0271
-0.20	14.725	0.994994	0.954614	-13.500	-0.0115	0.0250
-0.50	18.899	0.989688	0.958220	-13.748	-0.0118	0.0206
-1.00	26.103	0.984082	0.964379	-14.078	-0.0121	0.0159
-2.00	41.490	0.982584	0.977281	-14.732	-0.0125	0.0087
-3.50	68.181	0.983568	0.998176	-16.045	-0.0131	0.0047

The bandwidth was increased by over 400% before h exceeded the given limit. From Table 3 we can see that although decreasing A has the largest effect on B_3 of all the elliptic parameters, it also has the largest effect on h.

With this method exhausted, a second method was attempted. Starting from the same initial point, the derivatives of bandwidth with respect to three of the four elliptic arc parameters were used to determine the direction of the gradient of increasing bandwidth. A three-dimensional gradient vector of length k with components ΔA, ΔB, and Δb was determined using the following formulas:

$$\underline{\hspace{6cm}},$$

$$\underline{\hspace{6cm}},$$

$$\underline{\hspace{6cm}}.$$

The length of the gradient vector, k, was then incrementally increased and the change in each of the variables was recorded in Table 5.

Table 5. Results of incremental increase in k for several parameters ("gradient method").

k	B_3	e	h
0.10	13.418	0.997490	0.953280
0.20	14.956	0.995086	0.954440
0.50	19.371	0.989698	0.957726
1.00	27.079	0.983444	0.963388
2.00	43.301	0.979504	0.975299
3.50	69.948	0.976538	0.994670
3.75	74.713	0.976259	0.998152
3.80	75.747	0.976413	0.998884

For k values greater than 3.80, the value of h exceeded 0.999213, so calculations were stopped. Increasing the bandwidth using this gradient method was an improvement when compared with simply changing A, though not a large one.

A third method of broadening the bandwidth was then attempted. In this method, a two-dimensional vector of length k with components of ΔB and Δb was to be incrementally increased in the direction of the gradient, using the same starting point as the previous method. These two elliptic arc parameters were chosen because their initial $\partial h/\partial\_$ and $\partial e/\partial\_$ values were the lowest (see Table 3). It was thought that because these values were so low, B_3 could have larger increases before e or h exceeded the set limits. The components of the gradient vector, ΔB and Δb, were determined as follows:

$$\underline{\hspace{4cm}},$$

$$\underline{\hspace{4cm}}.$$

The length of the gradient vector, k, was then incrementally increased and the change in each of the variables was recorded in Table 6.

For k values greater than 7.00, the value of e exceeded 1.04999, so calculations were stopped. Increasing the bandwidth using this method also failed to yield better results than either of the previous two methods. The assumption that a low initial value of $\partial e/\partial k$ would predict

consistently small increases in *e* proved false in this case, as $\partial e/\partial k$ increased by a factor of 10 over the course of a 7 mm change in *k*. $\partial h/\partial k$, however, did remain fairly consistent throughout – increasing by only 0.0003 over the course of a 7 mm change in *k*.

Table 6. Results of incremental increase in *k* (corresponding to a change in *B* and *b*) for several parameters.

k	B_3	e	h	$\partial e/\partial k$	$\partial h/\partial k$
0.01	12.073	0.999998	0.952319	0.0007	0.0013
0.02	12.146	0.999995	0.952340	0.0002	0.0017
0.05	12.320	0.999962	0.952385	-0.0006	0.0016
0.10	12.557	0.999933	0.952461	-0.0006	0.0016
0.20	13.087	0.999879	0.952595	-0.0006	0.0014
0.50	14.705	0.999771	0.953039	-0.0004	0.0015
1.00	17.421	1.001393	0.953792	0.0014	0.0015
2.00	22.806	1.009676	0.955307	0.0048	0.0015
5.00	38.726	1.033939	0.960013	0.0068	0.0015
6.00	45.532	1.041768	0.962101	0.0070	0.0016
7.00	49.273	1.049858	0.963315	0.0071	0.0016

Of these methods, the gradient method was the most effective for an increase in B_3. All three methods, however, successfully proved that an increase in B_3 could be possible through the manipulation of elliptic arc parameters *A*, *B*, and *b*.

Broadening First Seven Dipole Modes

In SRF cavities, it is important to avoid "trapped modes", which occur at non-propagating frequencies. That is, it is important both to increase the bandwidths of each dipole mode (above the cutoff frequency, 1600 MHz) and to decrease the space between each band.

Several possible mathematical ways of writing this goal ("goal functions") were proposed. Ideally, the goal function, *G*, should be written in such a way that its optimization (maximization in our case) will help to achieve the goal of reducing the number of trapped modes. Below are two possible goal functions.

———

G_1 simply states that the net bandwidth should be as large as possible while G_2 emphasizes relative increases in bandwidth (where *i* refers to a new bandwidth and *o* refers to the initial bandwidth). G_1 was used in this

attempt to reduce the number of trapped modes due to its simplicity.

First, the bandwidths of each of the first seven dipole modes were calculated at the same initial point as in the previous section (where $\alpha = 90°$ and *e* = 1), as well as for ERL, TESLA, and reentrant cavities for comparison. Although the true number of dipole modes is infinite, our calculations were limited to the first seven modes because frequencies were limited to values below 4 GHz. These calculations were done using SLANS2 to analyze a half-cell geometry file created by TunedCell at an accuracy level of $1.0\cdot10^{-7}$ with boundary conditions modified to match each mode – for instance, a half-cell mesh of B_4's π-mode should have a magnetic boundary on its left side and an electric boundary on its right side. The half-cell fields are shown in Table 7 in the appendix. The half-cell mesh was used for convenience in this case because, as before, it was believed that only f_π and f_0 modes were necessary for bandwidth calculation.

Table 8. Initial bandwidths and G_1 for each of the seven dipole modes for 90°, reentrant, ERL and TESLA cavities.

	90°	RE	ERL	TESLA
B_1	195.877	196.303	178.635	173.394
B_2	102.024	103.759	70.354	62.352
B_3	14.064	7.080	87.590	107.451
B_4	286.023	291.641	232.265	215.784
B_5	55.038	54.973	50.148	47.790
B_6	6.987	5.760	16.992	17.710
B_7	442.660	438.907	484.957	487.394
G_1	1102.673	1098.423	1120.941	1111.875

From Table 8, we can see that the seven dipole modes have a wide range of possible bandwidths, with some bands very broad and others very narrow. In terms of the goal function, the ERL cavity has the best G_1 while the reentrant cavity has the worst, with our 90° cavity falling in the middle.

Next, as before, the derivatives of each bandwidth with respect to three of the four elliptic arc parameters (*A*, *B*, and *b*) were calculated by modifying each elliptic arc parameter, separately, by 0.01 mm and recording the changes in bandwidth. The derivatives of *e* and *h* with respect to these parameters were also calculated. All derivatives were recorded in Table 9.

Table 9. Various derivatives taken with respect to A, B, and b.

	$\partial B_n/\partial A$	$\partial B_n/\partial B$	$\partial B_n/\partial b$
B_1	15.7	-1.0	1.4
B_2	20.5	-1.7	1.1
B_3	-13.0	5.0	2.1
B_4	3.8	-5.0	-1.6
B_5	-3.5	0.8	-0.8
B_6	-6.2	0.8	0.0
B_7	-23.8	1.8	-0.3
	$\partial e/\partial\_$		$\partial h/\partial\_$
A	0.0309		-0.0072
B	-0.0007		0.0012
b	-0.0002		0.0009

The derivatives shown in Table 9 were used to create equations describing the change in each of the bandwidths (ΔB_n) corresponding to the change in each elliptic arc parameter. Formulas for Δe and Δh were created as well. Then, the Monte Carlo technique was used to estimate an optimized ΔG_1 value. That is, a random number generator was used to generate 10,000 random numbers in the range of (-0.1, 0.1) for each of ΔA, ΔB and Δb, which were then plugged in to the ΔB_n, Δe and Δh equations. Using these values, 10,000 ΔG_1 values were found, and of these, the largest ΔG_1 whose Δe and Δh values did not exceed 0.05 was recorded, as were its corresponding ΔA, ΔB and Δb values. These elliptic arc parameters were used by TunedCell to create a half-cell geometry file which was fed into SLANS2 to determine the actual ΔB values for each mode, and in turn the actual ΔG_1 value was determined. The predicted values were compared with these actual values for accuracy. This process was repeated three more times, with random number ranges increased to (-0.5, 0.5), (-1.0, 1.0), and finally (-5.0, 5.0). Data was recorded in Table 10.
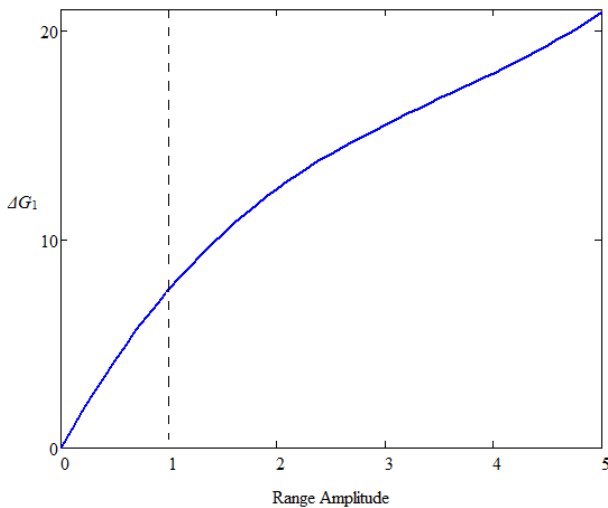

Figure 9. ΔG_1 plotted against the amplitude of the range of random numbers given to each elliptic arc parameter.

From Table 10, it is apparent that increasing the range of random numbers available to each of the elliptic arc parameters increases ΔG_1 but decreases the accuracy of the prediction, as indicated by the greater and greater differences between actual and predicted values as the range increases. The range was increased no further after (-5.0, 5.0) because it was assumed that the derivatives of bandwidth with respect to the various elliptic arc parameters had changed significantly from their original values in such a large range. Next, ΔG_1 was plotted against range to determine to what extent range should be allowed to increase for a given set of derivatives, as shown in Fig. 9.

Table 10. Predicted ΔB_n and ΔG_1 values compared to actual values for several ranges of random numbers given to each of the elliptic arc parameters.

	Predicted	Actual	Difference
(-0.1, 0.1)	ΔA = -0.0985, ΔB = 0.1000, Δb = 0.0937		
ΔB_1	-1.516	-1.506	0.010
ΔB_2	-2.087	-2.069	0.018
ΔB_3	1.977	1.998	0.021
ΔB_4	-1.024	-1.022	0.002
ΔB_5	0.350	0.325	-0.025
ΔB_6	0.691	0.678	-0.013
ΔB_7	2.497	2.501	0.004
ΔG_1	0.888	0.905	0.017
(-0.5, 0.5)	ΔA = -0.4967, ΔB = 0.4593, Δb = 0.4611		
ΔB_1	-7.612	-7.590	0.022
ΔB_2	-10.456	-10.390	0.066
ΔB_3	9.722	9.961	0.239
ΔB_4	-4.922	-4.932	-0.010
ΔB_5	1.737	1.302	-0.435
ΔB_6	3.447	3.101	-0.346
ΔB_7	12.510	12.753	0.243
ΔG_1	4.426	4.205	-0.221
(-1.0, 1.0)	ΔA = -0.9888, ΔB = 0.4902, Δb = 0.9626		
ΔB_1	-14.667	-14.721	-0.054
ΔB_2	-20.046	-20.000	0.046
ΔB_3	17.328	18.133	0.805
ΔB_4	-7.749	-7.891	-0.142
ΔB_5	3.083	1.651	-1.432
ΔB_6	6.523	5.280	-1.243
ΔB_7	24.128	25.150	1.022
ΔG_1	8.600	7.602	-0.998
(-5.0, 5.0)	ΔA = -3.0612, ΔB = -4.5832, Δb = 4.1551		
ΔB_1	-37.661	-39.215	-1.554
ΔB_2	-50.393	-52.097	-1.704
ΔB_3	25.606	32.861	7.255
ΔB_4	4.635	1.429	-3.206
ΔB_5	3.724	-4.368	-8.092
ΔB_6	15.313	9.091	-6.222
ΔB_7	63.361	73.180	9.819
ΔG_1	24.524	20.881	-3.643

From Fig. 9, one can see that the slope of ΔG_1 becomes less steep and linear when the range amplitude reaches

values greater than 1.0. This was thought to indicate that derivatives of bandwidth with respect to elliptic arc parameters should be recalculated from this point. These new derivatives were found as before, but with the (-1.0, 1.0) geometry as an initial point. The derivatives of e and h with respect to these parameters were also recalculated. Using the new derivatives, new values for ΔB_n and ΔG_1 were predicted for a (-1.0, 1.0) range from that point – or, (-2.0, 2.0) range from the original initial point. This process of recalculating derivatives for each 1.0 increase in range amplitude was repeated for (-3.0, 3.0), (-4.0, 4.0) and (-5.0, 5.0). Then, actual values were compared with these predicted values, and all values were recorded in Table 11.
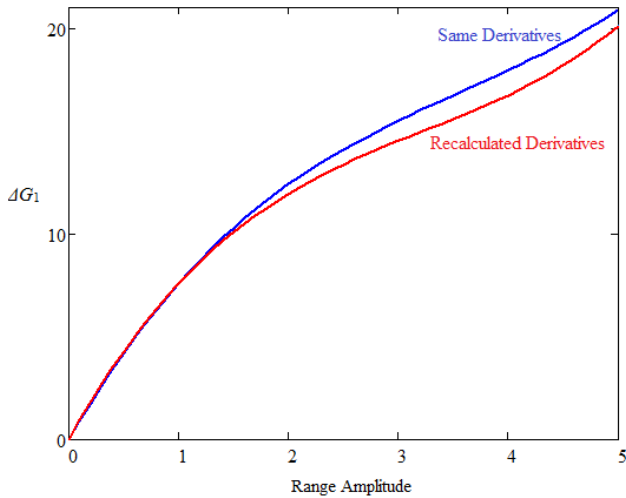

Figure 10. ΔG_1 plotted against the amplitude of the range of random numbers given to each elliptic arc parameter for both methods – keeping the same derivatives the entire time and recalculating derivatives for every 1.0 increase in range amplitude.

From Table 11, it is clear that the accuracy for these ΔG_1 predictions changes erratically despite the fact that derivatives for ΔB_n, e, and h with respect to the elliptic arc parameters were recalculated for each point. Moreover, the overall increase in G_1 for this procedure is only 20.100 MHz, which is actually less than the increase in G_1 achieved using the same derivatives the whole time, (20.881 MHz), as shown in Fig. 10. Hence, recalculating derivatives for every 1.0 increase in range amplitude doesn't yield improvement when compared with simply using the same derivatives the entire time.

Both of these methods yield very small increases compared with the original G_1 value (1102.673 MHz, from Table 8). However, both methods also yield better final G_1 values than the TESLA and ERL cavities (1120.941 MHz, 1111.875 MHz, from Table 8); using the same derivatives each time yields a final G_1 value of 1123.554 MHz and recalculating derivatives for each 1.0 increase in range yields a final G_1 of 1122.773 MHz. So both methods are successful in this respect, with the

"same derivatives" method slightly more successful. The dispersion curves for each dipole mode for the most improved goal function are shown in Fig 11.

Table 11. Predicted ΔB_n and ΔG_1 values compared to actual values for several ranges of random numbers, with derivatives recalculated at each point.

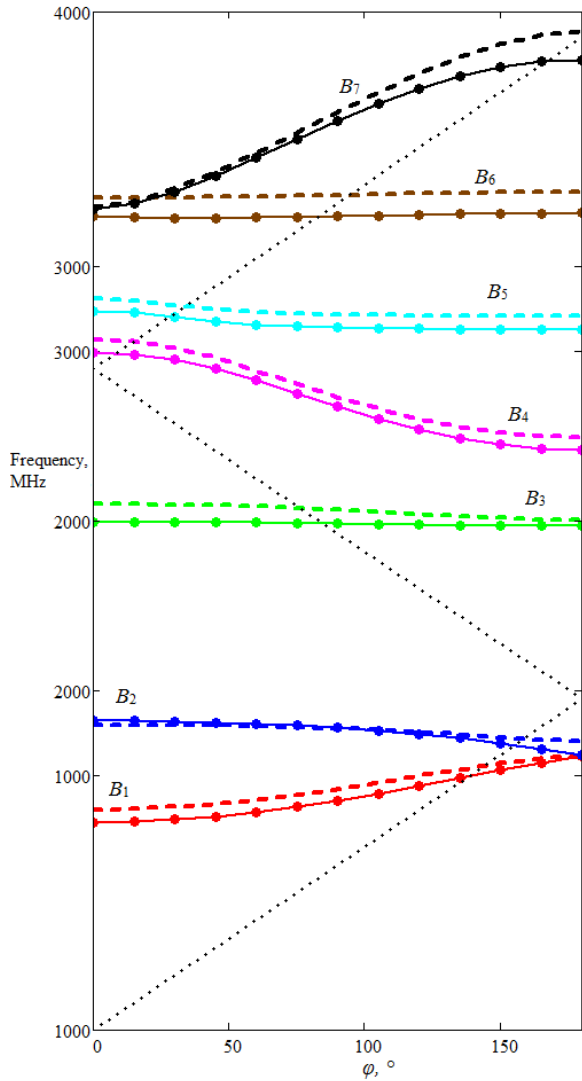|	Predicted	Actual	Difference
(-2.0, 2.0)	ΔA = -1.9741, ΔB = 1.4898, Δb = 1.8995		
ΔB_1	-29.170	-30.039	-0.869
ΔB_2	-40.780	-40.922	-0.142
ΔB_3	39.380	40.088	0.708
ΔB_4	-18.218	-18.349	-0.131
ΔB_5	2.085	0.374	-1.711
ΔB_6	9.616	8.270	-1.346
ΔB_7	51.903	52.518	0.615
ΔG_1	14.816	11.940	-2.876
(-3.0, 3.0)	ΔA = -2.9680, ΔB = 0.5820, Δb = 2.8828		
ΔB_1	-43.942	-43.939	0.003
ΔB_2	-59.057	-59.186	-0.129
ΔB_3	53.319	54.133	0.814
ΔB_4	-20.117	-20.377	-0.260
ΔB_5	-2.511	-3.472	-0.961
ΔB_6	9.480	8.919	-0.561
ΔB_7	77.795	78.446	0.651
ΔG_1	14.967	14.524	-0.443
(-4.0, 4.0)	ΔA = -2.0352, ΔB = -0.3732, Δb = 3.7811		
ΔB_1	-25.794	-26.134	-0.340
ΔB_2	-36.260	-36.540	-0.280
ΔB_3	35.015	35.595	0.580
ΔB_4	-13.494	-13.374	0.120
ΔB_5	1.032	-0.783	-1.815
ΔB_6	9.468	8.189	-1.279
ΔB_7	49.269	49.793	0.524
ΔG_1	19.236	16.746	-2.490
(-5.0, 5.0)	ΔA = -3.0333, ΔB = -1.1896, Δb = 4.9606		
ΔB_1	-40.104	-40.145	-0.041
ΔB_2	-54.893	-55.006	-0.113
ΔB_3	49.483	50.117	0.634
ΔB_4	-15.865	-16.014	-0.149
ΔB_5	-2.917	-4.124	-1.207
ΔB_6	10.031	9.333	-0.698
ΔB_7	75.288	75.939	0.651
ΔG_1	21.023	20.100	-0.923

Figure 11. Dispersion curves for the 90°-cavity improved by the Monte Carlo technique (without changing derivatives) for each of the first seven dipole modes, with frequency plotted against phase shift. Original curves are included for comparison and shown as solid lines, while improved curves are dashed lines. Dotted lines show Brillouin light lines.

The Sixth Dipole Mode

During, earlier calculations, it was mentioned that only f_0 and f_π were thought to be necessary for calculating the bandwidth of a given band. In fact, the standard formula for calculating bandwidth throughout this paper has been $B = |f_0 - f_\pi|$. The sixth dipole mode, however, is a case where this does not appear to hold true.

From Fig. 11, B_6 looks like a straight line compared with the other, broader bandwidths. When the B_6 dispersion curve is examined more closely, however, we see that its shape is strange. That is, the assumption underlying the $B = |f_0 - f_\pi|$ formula is that one of f_0 and f_π should be the

maximum frequency in the band and one should be the minimum. From Fig. 12, however, it is clear that this is not the case for B_6. Although the maximum frequency occurs when $\varphi = \pi$, the minimum frequency occurs at $f_{\pi/4}$, not f_0. A true bandwidth calculation for this mode would be $B_6 = |f_\pi - f_{\pi/4}|$, which yields more than double the B_6 value of the original formula (14.312, compared with 6.987).
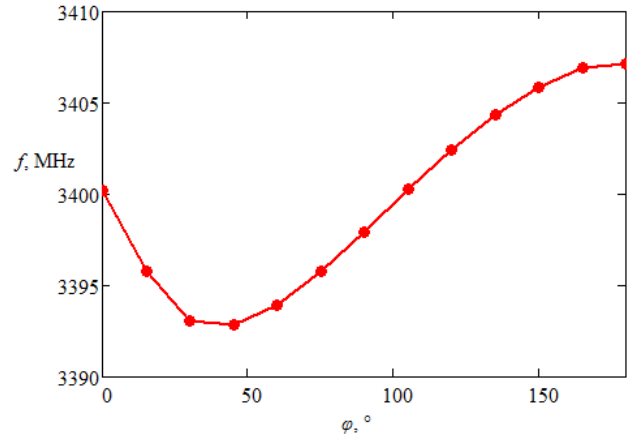

Figure 12. Dispersion curve plotting dependence of frequency on phase shift for the sixth dipole mode.

So a more accurate measure of bandwidth than the $B = |f_0 - f_\pi|$ formula must be devised. Ideally, bandwidth should be determined by the highest and lowest frequency of each mode, but describing an algorithm for this calculation could be difficult if minimums and maximums appear in unexpected places as in B_6. For now, a new formula could simply be $B = f_{max} - f_{min}$, which coincides with the original bandwidth formula in each of the seven dipole modes but the sixth. Furthermore, the assumption from earlier on in the paper that calculating a single- or half-cell geometry is enough to determine the bandwidth of each HOM appears to be false, as a six-cell geometry is necessary to calculate $f_{\pi/4}$.

SUMMARY

For a 90°-cavity with constraints on the upper limits of e and h, several methods of reducing trapped modes are described. These methods entail both broadening a single mode and broadening the sum of all higher-order modes through modification of the elliptic arc parameters A, B, a and b. The most successful method of broadening a single mode (the third dipole mode) was increasing changes in the elliptic arc parameters in the direction of the gradient of increasing B_3. This method increased B_3 from 12.025 MHz to 75.746 MHz before h exceeded its limit. For broadening the sum of all dipole modes, the most successful method was using the derivatives of each bandwidth with respect to each elliptic arc parameter to determine a goal function equation, and then using the Monte Carlo technique to optimize this equation without exceeding the e or h limits. This method increased the

sum of all dipole mode bandwidths from 1102.673 MHz to 1123.554 MHz, a value slightly larger than TESLA or ERL's HOM bandwidth sum.

However, examination of the sixth dipole mode's dispersion curve shows that we may need to use a different method of calculating bandwidth in the future to obtain more accurate results for bandwidth increases, possibly invalidating some earlier data.

AKNOWLEDGEMENTS

REFERENCES

[1] H. Padamsee *et al.*, *RF Superconductivity for Accelerators* (John Wiley & Sons, New York, 1998).

[2] V. Shemelin. Optimal choice of cell geometry for a multicell superconducting cavity. *Physical Review Special Topics – Accelerators and Beams* **12** 114701 (2009).

[3] Z. Li and C. Adolphsen. A new SRF cavity shape with minimized surface electric and magnetic fields for the ILC. In *Proceedings of LINAC08*, Victoria, BC, Canada.

[4] N. Juntong, R. M. Jones, and I. R. R. Shinton. SRF cavity geometry optimization for the ILC with minimized surface E.M. fields and superior bandwidth. In *Proceedings of EPAC08.* Genoa, Italy.

[5] D. G. Myakishev and V. P. Yakovlev, in *Proceedings of the Particle Accelerator Conference*, Dallas, TX, 1995 (IEEE, New Jersey, 1995), pp. 2348 – 2350.

[6] D. Myakishev. TunedCell. Cornell SRF Group Internal Report No. SRF 942008-13, 1994.

APPENDIX

Table 7. π and 0 modes for the first seven dipole bands of a 90°-cavity.

Band	Boundary Conditions			
	Magnetic, Magnetic	**Magnetic, Electric**	**Electric, Magnetic**	**Electric, Electric**
1, 2	$B_1, 0$	B_2, π	B_1, π	$B_2, 0$
3, 4	$B_3, 0$	B_4, π	B_3, π	$B_5, 0$
5, 6	$B_4, 0$	B_5, π	B_6, π	$B_6, 0$
7, 8	$B_7, 0$	B_8, π	B_7, π	$B_8, 0$